Numerical Simulation of Cohesive Fracture by the Virtual-Internal-Bond Model

P. Zhang [1], P. Klein[2], Y. Huang[1,3], H. Gao[4] and P. D. Wu [5]

Abstract: The recently developed virtual-internal-bond (VIB) model has incorporated a cohesive-type law into the constitutive law of solids such that fracture and failure of solids become a coherent part of the constitutive law and no separate fracture or failure criteria are needed. A numerical algorithm is developed in this study for the VIB model under static loadings. The model is applied to study three examples, namely the crack nucleation and propagation from stress concentration, kinking and subsequent propagation of a mode II crack, and the buckling-driven delamination of a thin film from a substrate. The results have demonstrated that the VIB model provides an effective method to study crack nucleation and propagation in engineering materials and systems.

1 Introduction

Cohesive surface modeling of fracture (Barenblatt, 1959; Dugdale, 1960; Willis, 1967) started more than 30 years ago. Significant efforts are made in recent years to simulate fracture initiation and crack growth by cohesive surface models, in which a set of discrete cohesive surfaces having finite work of fracture and finite cohesive strength is introduced at the stage of finite element discretization. Nonlinear cohesive laws that dictate the relation between the tractions and separations are prescribed at element boundaries. Once the work of fracture and cohesive strength are reached, cracks are allowed to form and propagate along element boundaries in accordance with the cohesive laws. Therefore, a separate and external fracture criterion (e.g., K_{IC}, G_{IC}) is not needed in the cohesive surface modeling of fracture since the frac-

ture criterion has been implicitly built into the cohesive laws. The cohesive surface models have been successfully applied to simulate dynamic crack tip instabilities (Xu and Needleman, 1994), material fragmentation (Camacho and Ortiz, 1996; Espinosa *et al*, 1998), impact-induced delamination of composites (Geubelle and Baylor, 1998) and quasi-brittle fracture of solids (Tijssens *et al*, 2000).

There are other cohesive fracture models such as the embedded-process-zone model (Tvergaard and Hutchinson, 1992, 1993), which accounts for the effort of plasticity inside the volumetric elements. Gao and Klein (1998) and Klein and Gao (1998, 2000) proposed a virtual-internal-bond (VIB) model to incorporate a cohesive-type law directly into the constitutive law by statistically averaging a spatial network of cohesive bonds connecting randomly distributed material particles within the material (Figure 1). Each bond can be described by a bond energy function $U(l)$, where l denotes the bond length. Its derivative, $U'(l)$, gives the cohesive force in the bond. The macroscopic collective behavior of this random bond network is determined by the so-called Cauchy-Born rule of crystal elasticity, i.e., by equating the macroscopic strain energy function on the continuum level to the potential energy stored in the cohesive bonds on the microscale. For an imposed deformation at a point (e.g., the Green-Lagrange strain E_{IJ}), the stretch in cohesive bonds can be calculated once the bond orientations are known, as shown in Fig. 1. The summation of bond energy over all microscopic cohesive bonds at the same material point provides the macroscopic strain energy function. Its derivative with respect to the Green-Lagrange strain E_{IJ} gives the second Piola-Kirchhoff stress S_{IJ}. The macroscopic constitutive law is then obtained from the cohesive law of microscopic bonds. Furthermore, no presumed or separate fracture criteria are needed in the VIB model since it has implicitly embedded the fracture criterion into the constitutive law. Fracture can be simply viewed as the strain localization (Klein and Gao, 1998, 2000).

[1] Department of Mechanical and Industrial Engineering, University of Illinois, Urbana, IL 61801

[2] Sandia National Laboratories, Livermore, CA 94551

[3] Corresponding author; email: huang9@uiuc.edu; fax: (217) 244-6534

[4] Division of Mechanics and Computation, Stanford University, Palo Alto, CA 94305

[5] Alcan International Limited, P.O. Box 8400, Kingston, Ontario K7L 5L9, Canada
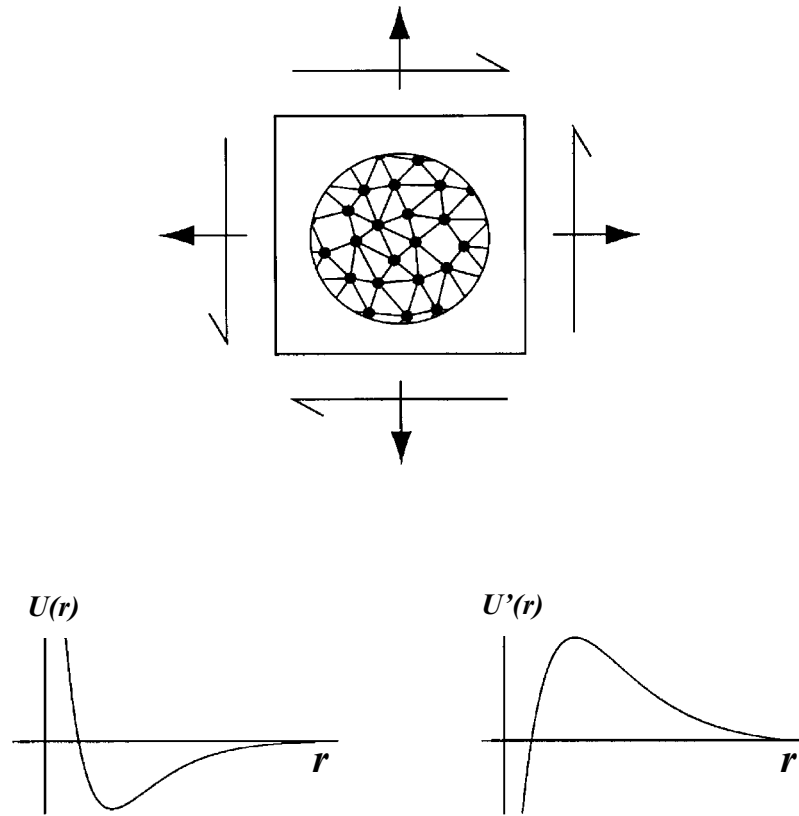
$$F = \frac{\partial x}{\partial X} \quad \rightarrow \quad E = \frac{1}{2}(F^T F - I) \quad \rightarrow \quad stretch \quad l = l_0 \sqrt{1 + 2\xi_I E_{IJ} \xi_J}$$

$$\downarrow$$

$$\Phi = \langle U(l) \rangle \quad \leftarrow \quad Bond\,potential\,energy\,U(l)$$

Figure 1 : The VIB model with randomized internal bonds and a schematic diagram to establish the macroscale constitutive law from microscopic bond energy function

The softening behavior in the cohesive force law, $U'(l)$, on the microscale (Figure 1) translates to macroscopic softening behavior of materials at relatively large deformation, which may lead to difficulties in numerical simulations. This does not seem to be a significant problem in dynamic simulations nor for material systems containing weak interfaces (Gao and Klein, 1998; Klein and Gao, 1998, 2000). However, for homogeneous materials subjected to static loading, the Newton-Rhapson method used to solve nonlinear equations iteratively may not always provide a convergent solution for the static VIB model. The purpose of this paper is to develop a robust numerical algorithm for the static VIB model so as to expand the model's application range to static engineering problems, as demonstrated through numerical examples in the paper. We begin with a summary of the VIB model (Gao and Klein, 1998) in Section 2. For isotropic solids, Klein and Gao (2000) has developed a formulation that is much more efficient for numerical simulations. This formulation is summarized in Section 3. The numerical algorithms and their implementation on the ABAQUS finite element program are discussed in Section 4, while three numerical examples, namely the crack nucleation and propagation from stress concentration around a hole, mode II crack kinking and subsequent propagation, and the buckling-driven delamination of a thin film from the substrate, are presented in Section 5.

2 The Virtual-Internal-Bond Model

2.1 Macroscopic Strain vs. Microscopic Bond Stretch

The virtual-internal-bond (VIB) model proposed by Gao and Klein (1998) is established within the framework of hyperelasticity in continuum mechanics. The material points in the initial, undeformed configuration are described by the reference, Lagrangian coordinates $\mathbf{X} = (X_1, X_2, X_3)$, while the same material points in the current, deformed configuration are described by the spatial, Eulerian coordinates $\mathbf{x} = (x_1, x_2, x_3)$. In general, the relation between these two sets of coordinates, $\mathbf{x} = \mathbf{x}(\mathbf{X}, t)$, is completely determined by the deformation gradient tensor

$$\mathbf{F} = \frac{\partial \mathbf{x}}{\partial \mathbf{X}}, \qquad F_{iI} = \frac{\partial x_i(X_1, X_2, X_3, t)}{\partial X_I}, \qquad (1)$$

where t is time. The right Cauchy-Green tensor $\mathbf{C}$ and the Green-Lagrange strain tensor $\mathbf{E}$ are related to the deformation gradient tensor $\mathbf{F}$ by

$$\mathbf{C} = \mathbf{F}^{\mathrm{T}} \cdot \mathbf{F}, \qquad C_{IJ} = F_{iI} F_{iJ}, \qquad (2)$$

$$\mathbf{E} = \frac{1}{2}(\mathbf{C} - \mathbf{I}) = \frac{1}{2}(\mathbf{F}^{\mathrm{T}} \cdot \mathbf{F} - \mathbf{I}),$$
$$E_{IJ} = \frac{1}{2}(C_{IJ} - \delta_{IJ}) = \frac{1}{2}(F_{iI} F_{iJ} - \delta_{IJ}). \qquad (3)$$

Once the strain tensor $\mathbf{E}(\mathbf{X})$ at a material point $\mathbf{X}$ is known, the stretch in a direction ξ at $\mathbf{X}$ is $[1 + 2\xi \cdot \mathbf{E}(\mathbf{X}) \cdot \xi]^{\frac{1}{2}}$ (e.g., Marsden and Hughes, 1983). As shown in Figure 1, each material point on the macroscale is attached to bonds on the microscale. Therefore, the bond which has the initial, unstretched length l_0 is now stretched to

$$l = l_0 [1 + 2\xi \cdot \mathbf{E}(\mathbf{X}) \cdot \xi]^{\frac{1}{2}} = l_0 [1 + 2\xi_I E_{IJ} \xi_J]^{\frac{1}{2}}, \qquad (4)$$

where ξ is the unit vector along the bond direction on the microscale, and $\mathbf{E}(\mathbf{X})$ is the macroscopic strain at the material point $\mathbf{X}$. It should be pointed out that the stretched bond length depends on both the macroscopic strain $\mathbf{E}(\mathbf{X})$ and the microscopic bond orientation ξ.

2.2 Macroscopic Strain Energy Function vs. Microscopic Bond Potential Energy

The potential energy stored in each bond is denoted by $U(l)$, where the stretched bond length l is given in (4). The macroscopic strain energy per unit undeformed volume in this network of cohesive bonds can be obtained via the Cauchy-Born rule (Milstein, 1980; Tadmor *et al*, 1996), i.e., by equating the macroscopic strain energy function at a material point $\mathbf{X}$ to the potential energy of all microscopic bonds attached to the same material point. This gives the strain energy function $\Phi(E_{IJ})$,

$$\Phi(E_{IJ}) = \langle U(l) \rangle = \left\langle U(l_0 \sqrt{1 + 2\xi_I E_{IJ} \xi_J}) \right\rangle, \qquad (5)$$

where $\langle \cdots \rangle$ stands for the average over all bonds at $\mathbf{X}$. If one further assumes that the bonds have identical initial length l_0, $\langle \cdots \rangle$ becomes the average over all orientations ξ of the bonds. For a three-dimensional problem, this average is given by

$$\langle \cdots \rangle = \int_0^{2\pi} \int_0^{\pi} (\cdots) D_0(\theta, \phi) \sin \theta \, d\theta d\phi, \qquad (6)$$

where θ and ϕ are angles in spherical coordinates, and $D_0(\theta,\phi)$ is the bond density such that $D_0(\theta,\phi)\sin\theta\,d\theta d\phi$ is the number of bonds per unit reference volume with bond angles in the range $(\theta,\theta+d\theta)$ and $(\phi,\phi+d\phi)$. For an isotropic solid with fully randomized internal bonds, $D_0(\theta,\phi)$ becomes a constant D_0, independent of θ and ϕ. According to (6), the strain energy function Φ in three-dimension becomes

$$\Phi(E_{IJ}) = D_0 \int_0^{2\pi} \int_0^{\pi} U(l_0\sqrt{1+2\xi_I E_{IJ}\xi_J})\sin\theta\,d\theta d\phi, \quad (7)$$

where the unit vector ξ along the bond direction is given by

$$\xi = (\xi_1,\xi_2,\xi_3) = (\sin\theta\cos\phi,\sin\theta\sin\phi,\cos\theta). \quad (8)$$

For a two-dimensional plane-stress problem with fully randomized internal bonds within the plane, the bond density takes the form of $D_0(\phi)\,\delta(\theta-\frac{\pi}{2})$, such that the average $\langle\cdots\rangle$ becomes

$$\langle\cdots\rangle = \int_0^{2\pi} (\cdots)\,D_0(\phi)\,d\phi, \quad (9)$$

where ϕ is the polar angle in the plane. For fully randomized bonds, $D_0(\phi)$ is a constant D_0 and the strain energy function Φ becomes

$$\Phi(E_{IJ}) = D_0 \int_0^{2\pi} U(l_0\sqrt{1+2\xi_I E_{IJ}\xi_J})\,d\phi, \quad (10)$$

where $\xi = (\xi_1,\xi_2) = (\cos\phi,\sin\phi)$.

Equations (7) and (10) give the macroscopic strain energy function Φ in terms of the microscopic bond potential energy U for an isotropic solid with fully randomized internal bonds.

2.3 Macroscopic Stress and Moduli

Once the strain energy function $\Phi(E_{IJ})$ is known, the second Piola-Kirchhoff stresses S_{IJ} and moduli C_{IJKL} are readily to be obtained as (Gao and Klein, 1998)

$$S_{IJ} = \frac{\partial\Phi}{\partial E_{IJ}} = l_0^2 \left\langle \frac{U'(l)}{l}\xi_I\xi_J \right\rangle, \quad (11)$$

$$\begin{aligned}
\mathsf{C}_{IJKL} &= \frac{\partial S_{IJ}}{\partial E_{KL}} = \frac{\partial^2\Phi}{\partial E_{IJ}\partial E_{KL}} \\
&= l_0^4 \left\langle \left(\frac{U''(l)}{l^2} - \frac{U'(l)}{l^3}\right)\xi_I\xi_J\xi_K\xi_L \right\rangle,
\end{aligned} \quad (12)$$

where the stretched bond length l is given in (4), and the averaging scheme $\langle\cdots\rangle$ is defined in (6) or (9). Once expression of the bond potential energy $U(l)$ is known, Equation (11) provides the macroscopic stress-strain relation for the VIB model, while the moduli in (12) are useful in the incremental stress-strain relation. It is observed that the moduli in (12) have the Cauchy symmetry $\mathsf{C}_{IJKL} = \mathsf{C}_{JIKL} = \mathsf{C}_{IJLK} = \mathsf{C}_{KLIJ} = \mathsf{C}_{IKJL}$. Moreover, it can be shown that the pure volumetric deformation $E_{IJ} = \varepsilon\delta_{IJ}$ gives only a pure volumetric hydrostatic stress, $S_{IJ} = \sigma\delta_{IJ}$.

2.4 Modeling Fracture as Strain Localization

Even though it is not necessary to impose a separate and external fracture criterion in the VIB model, it is important to identify a fracture indicator in order to determine some key quantities related to fracture, such as the crack tip location and speed, and the zone over which fracture has occurred. Unlike a fracture criterion in classical fracture mechanics, a fracture indicator in the VIB model does not intervene the continuum stress analysis even after fracture occurs.

Hill (1962) described the loss of strong ellipticity of the strain energy density function as an indication of material instability, which typically occurs in the form of strain localization and leads to the final failure of the material. The classical condition for strain localization is characterized by the acoustical tensor $\mathbf{Q}(\mathbf{N})$ being singular (Hill, 1962; Truesdell and Noll, 1965; Armero and Garikipati, 1996; Klein and Gao, 1998), i.e.,

$$det[\mathbf{Q}(\mathbf{N})] = 0, \quad (13)$$

where det is the determinant of the second order tensor, the acoustical tensor $\mathbf{Q}(\mathbf{N})$ is given by

$$Q_{ik} = B_{iJkL}N_J N_L, \quad (14)$$

$\mathbf{N}$ is the unit vector for an arbitrary direction, and $\mathbf{B}$ is given in terms of incremental modulus tensor C, deformation gradient $\mathbf{F}$ and the second Piola-Kirchhoff stress $\mathbf{S}$ by

$$B_{iJkL} = \mathsf{C}_{IJKL}F_{iI}F_{kK} + S_{JL}\delta_{ik}. \quad (15)$$

In other words, if there exists a direction $\mathbf{N}$ such that the acoustical tensor becomes singular, strain localization starts.

One difference between the VIB model and the cohesive surface model is that the former is established through the constitutive modeling of solids. Numerical implementation of the VIB model in a finite element program does not involve additional (surface) elements nor additional degrees of freedom. Crack nucleation and propagation can be viewed as strain localization in the VIB model, i.e., very large deformation around localized and concentrated regions (Klein and Gao, 1998, 2000). However, it is unclear how to determine the crack tip location, speed, and crack propagation path in such an approach. Klein and Gao (1998, 2000) suggested using the strain localization condition (13) as a fracture indicator to determine the crack tip location and crack propagation path. This indicator is adopted in the present study. Further details are given in section 4.

2.5 *Phenomenological Cohesive Force Law of Microscopic Bonds*

Following Gao and Klein (1998), we adopt a simple, two-parameter phenomenological cohesive force law

$$U'(l) = A(l - l_0) \exp\left(-\frac{l - l_0}{Bl_0}\right), \tag{16}$$

where l_0 is the initial, unstretched bond length; A is the slope of $U'(l)$ for the unstretched bond (Figure 2) and is linearly proportional to the shear modulus μ of the solid. With the plane stress model, the shear modulus for infinitesimal deformations is (Gao and Klein, 1998; Klein and Gao, 1998, 2000)

$$\mu = \frac{\pi}{4} D_0 l_0^2 A. \tag{17}$$

The parameter B in (16) is the critical stretch at which the maximum bond strength is reached (Figure 2); the larger B is the later the softening occurs in the bond. In other words, B is the percentage of stretch at which the softening starts. In a plane-stress state with equibiaxial stretching, $E_{IJ} = \varepsilon \delta_{IJ}$ $(I, J = 1, 2)$, the strain at which localization occurs, or equivalently, at which the maximum stress is reached, is given by (Gao and Klein, 1998)

$$\varepsilon^* = \frac{-1 + 2B + \sqrt{1 + 4B}}{4} = B + O\left(B^2\right), \tag{18}$$

i.e., B represents the localization strain.

Klein and Gao (2000) derived the elastic moduli in three-dimensional infinitesimal deformation in terms of the parameters of the cohesive potential. The bond density D_0,
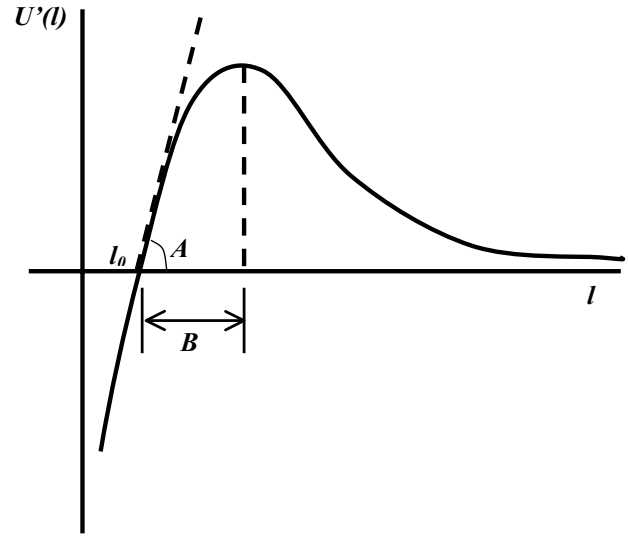

Figure 2 : A phenomenological cohesive force law

unstretched bond length l_0 always appear together with the parameter A in the combination of $D_0 l_0^2 A$, as in (17). Therefore, it is not necessary to prescribe D_0, l_0^2 and A separately.

3 VIB Model for Isotropic Solids

The constitutive law in the VIB model involves integrations of bond stretches and bond density function with respect to spherical angles or polar angles. For isotropic solids, the general VIB model can be recast to a new formulation which is much more efficient and better suited for numerical implementation (Klein and Gao, 2000). It ensures the isotropy of the constitutive law, regardless of the numerical integration scheme with respect to spherical or polar angles.

The right Cauchy-Green tensor $\mathbf{C}$ in (2) can be expressed in terms of its spectral decomposition along the principal stretch directions for an isotropic solid,

$$\mathbf{C} = \sum_{A=1}^{n_{sd}} \lambda_A^2 \mathbf{N}^{(A)} \otimes \mathbf{N}^{(A)}, \qquad C_{IJ} = \sum_{A=1}^{n_{sd}} \lambda_A^2 N_I^{(A)} N_J^{(A)}, \tag{19}$$

where $n_{sd} = 2$ *or* 3 for two or three dimension analysis, respectively, λ_A are the principal stretches (or equivalently, λ_A^2 are the eigenvalues of $\mathbf{C}$), and $\mathbf{N}^{(A)}$ are the corresponding unit vectors in the principal directions associated with λ_A. The Green-Lagrange strains in (3) be-

come

$$\mathbf{E} = \frac{1}{2}\sum_{A=1}^{n_{sd}}\left(\lambda_A^2 - 1\right)\mathbf{N}^{(A)}\otimes\mathbf{N}^{(A)}. \tag{20}$$

The strain energy function $\Phi(E_{IJ})$ can be written in terms of the principal stretches due to isotropy (Simo and Taylor, 1991),

$$\Phi(\mathbf{E}) = \hat{\Phi}(\lambda_A) \qquad (A = 1,\ldots,n_{sd}) \tag{21}$$

such that the second Piola-Kirchhoff stresses in (11) are given by

$$S_{IJ} = \frac{\partial\Phi}{\partial E_{IJ}} = 2\frac{\partial\Phi}{\partial C_{IJ}} = 2\sum_{A=1}^{n_{sd}}\frac{\partial\hat{\Phi}}{\partial\lambda_A}\frac{\partial\lambda_A}{\partial C_{IJ}}. \tag{22}$$

The last term in (22) for the case of distinct eigenvalues is (Simo and Taylor, 1991)

$$\frac{\partial\lambda_A}{\partial\mathbf{C}} = \frac{1}{2}\lambda_A\mathbf{M}^{(A)}, \qquad \frac{\partial\lambda_A}{\partial C_{IJ}} = \frac{1}{2}\lambda_A M_{IJ}^{(A)}, \tag{23}$$

where $\mathbf{M}^{(A)}$ is given by

$$\mathbf{M}^{(A)} = \frac{1}{\lambda_A^2}\mathbf{N}^{(A)}\otimes\mathbf{N}^{(A)}, \qquad M_{IJ}^{(A)} = \frac{1}{\lambda_A^2}N_I^{(A)}N_J^{(A)}. \tag{24}$$

The other term, $\frac{\partial\hat{\Phi}}{\partial\lambda_A}$, in (22) can be obtained for the isotropic VIB model by differentiating (5) with respect to λ_A (Klein and Gao, 2000),

$$\frac{\partial\hat{\Phi}}{\partial\lambda_A} = l_0^2\lambda_A\left\langle\frac{U'(l)}{l}\hat{\Xi}_A^2\right\rangle, \tag{25}$$

where $\langle\cdots\rangle$ stands for the average over spherical angles in (6) or polar angle (9), $\hat{\Xi}_A = \xi_I^{(A)}N_I^{(A)}$ is the projection (or component) of the unit directional vector ξ of the bond along the principal stretch direction $\mathbf{N}^{(A)}$, and the stretched length l in (4) becomes

$$l = l_0\left[\sum_{A=1}^{n_{sd}}\lambda_A^2\hat{\Xi}_A^2\right]^{\frac{1}{2}}. \tag{26}$$

Equations (22)-(25) can be rearranged to give stresses in terms of the principal stretches in the isotropic VIB model as

$$\mathbf{S} = \sum_{A=1}^{n_{sd}}S_A\lambda_A^2\mathbf{M}^{(A)}, \qquad S_{IJ} = \sum_{A=1}^{n_{sd}}S_A\lambda_A^2 M_{IJ}^{(A)}, \tag{27}$$

where

$$S_A = \frac{1}{\lambda_A}\frac{\partial\hat{\Phi}}{\partial\lambda_A} = l_0^2\left\langle\frac{U'(l)}{l}\hat{\Xi}_A^2\right\rangle. \tag{28}$$

The differentiation of (27) gives the incremental moduli as

$$\begin{aligned}
\mathsf{C}_{IJKL} &= \frac{\partial S_{IJ}}{\partial E_{KL}} = 2\frac{\partial S_{IJ}}{C_{KL}} \\
&= \sum_{A,B=1}^{n_{sd}}\gamma_{AB}\lambda_A^2\lambda_B^2 M_{IJ}^{(A)}M_{KL}^{(B)} \\
&\quad + 2\sum_{A=1}^{n_{sd}}S_A\lambda_A^2\left(M_{IJ}^{(A)}M_{KL}^{(A)} + T_{IJKL}^{(A)}\right), \\
\mathsf{C} &= \sum_{A,B=1}^{n_{sd}}\gamma_{AB}\lambda_A^2\lambda_B^2\mathbf{M}^{(A)}\otimes\mathbf{M}^{(B)} \\
&\quad + 2\sum_{A=1}^{n_{sd}}S_A\lambda_A^2\left(\mathbf{M}^{(A)}\otimes\mathbf{M}^{(A)} + \mathbf{T}^{(A)}\right), \tag{29}
\end{aligned}$$

where

$$\begin{aligned}
\gamma_{AB} = \gamma_{BA} &= \frac{1}{\lambda_B}\frac{\partial}{\partial\lambda_B}\left(\frac{1}{\lambda_A}\frac{\partial\hat{\Phi}}{\partial\lambda_A}\right) \\
&= l_0^4\left\langle\left(\frac{U''(l)}{l^2} - \frac{U'(l)}{l^3}\right)\hat{\Xi}_A^2\hat{\Xi}_B^2\right\rangle, \tag{30}
\end{aligned}$$

$\mathbf{T}^{(A)} = \frac{\partial\mathbf{M}^{(A)}}{\partial\mathbf{C}}$ is a fourth order tensor given in the Appendix. Besides the significant reduction in computational work, the isotropic VIB model also ensures the isotropy of the incremental moduli regardless of the numerical integration scheme, as compared to the general VIB model in the previous section. In other words, the formulation produces response that is invariant with transformations of the deformation gradient $\mathbf{F}\to\mathbf{FR}$, where $\mathbf{R}$ represents a right, orthogonal transformation, i.e., $\mathbf{R}^{\mathrm{T}}\mathbf{R} = \mathbf{1}$, $1_{IJ} = \delta_{IJ}$.

4   Numerical Implementation

4.1   Spatial Representation of the VIB Model

The general VIB model in Section 2 as well as the isotropic VIB model in Section 3 have been implemented in the ABAQUS finite element program through a USER-MATERIAL subroutine UMAT. The current state variables as well as strain increments are provided to UMAT, which then calculates the Jacobian matrix (incremental moduli) and updates all state variables. However,

ABAQUS uses the Cauchy (true) stress σ, instead of the second Piola-Kirchhoff stress $\mathbf{S}$, as the stress measure. Accordingly, stresses and incremental moduli established in Sections 2 and 3 have been recast in terms of the Cauchy stress, its Jaumann rate and the rate of deformation. A fully implicit time integration scheme has been adopted for this nonlinear problem.

Rather than making use of the transformation relation, $\sigma = \frac{1}{J}\mathbf{FSF}^{\mathrm{T}}$, the formulations in Section 3 can be transformed analytically to the corresponding spatial representations, where $\mathbf{F}$ is the deformation gradient, and $J = det(\mathbf{F})$. This significantly reduces the computational effort as compared to the numerical transformation from material to spatial representations. Since the deformation gradient $\mathbf{F}$ is provided to the USER-MATERIAL subroutine UMAT in ABAQUS, the left Cauchy-Green tensor is readily obtained as $\mathbf{b} = \mathbf{FF}^{\mathrm{T}}$, which has the same eigenvalues λ_A^2 as the right Cauchy-Green tensor $\mathbf{C}$ in (2), and the corresponding eigenvectors $\mathbf{n}^{(A)}$ are related to $\mathbf{N}^{(A)}$ associated with $\mathbf{C}$ by $\mathbf{n}^{(A)} = \mathbf{FN}^{(A)}$. Similar to (24), we define

$$\mathbf{m}^{(A)} = \mathbf{n}^{(A)} \otimes \mathbf{n}^{(A)}, \tag{31}$$

which is the direct transformation of $\mathbf{M}^{(A)}$ by $\mathbf{m}^{(A)} = \mathbf{FM}^{(A)}\mathbf{F}^{\mathrm{T}}$. The spatial representations of stresses and moduli are readily obtained from the transformation of (27) and (29),

$$\sigma_{ij} = \frac{1}{J}\sum_{A=1}^{n_{sd}} S_A \lambda_A^2 m_{ij}^{(A)}, \tag{32}$$

$$\begin{aligned}
c_{ijkl} &= \frac{1}{J}F_{iI}F_{jJ}F_{kK}F_{lL}C_{IJKL} \\
&= \frac{1}{J}\sum_{A,B=1}^{n_{sd}} \gamma_{AB}\lambda_A^2 \lambda_B^2 m_{ij}^{(A)} m_{kl}^{(B)} \\
&\quad + \frac{2}{J}\sum_{A=1}^{n_{sd}} S_A \lambda_A^2 \left(m_{ij}^{(A)} m_{kl}^{(A)} + t_{ijkl}^{(A)} \right),
\end{aligned} \tag{33}$$

where $t_{ijkl}^{(A)} = F_{iI}F_{jJ}F_{kK}F_{lL}T_{IJKL}^{(A)}$ is the transformation of the tensor $\mathbf{T}^{(A)}$ given in the Appendix, and it can be expressed analytically in terms of $\mathbf{b}$ and $\mathbf{m}^{(A)}$ (Klein and Gao, 2000) instead of computing from the above transformation.

4.2 Determination of Principal Stretches and Their Directions

The determination of the eigenvalues λ_A^2 and the corresponding eigenvectors $\mathbf{n}^{(A)}$ are straightforward because the deformation gradient $\mathbf{F}$ is provided to the USER-MATERIAL subroutine UMAT in ABAQUS, and the left Cauchy-Green tensor is readily evaluated from $\mathbf{b} = \mathbf{FF}^{\mathrm{T}}$. The equation for λ_A^2 is a third-order polynominal for three dimension and a quadratic equation for two dimension, for which the closed-form solutions can be found. The corresponding eigenvectors $\mathbf{n}^{(A)}$ can also be found analytically.

4.3 Average with Respect to Bond Angles

The average over the bond orientations becomes an integral with respect to spherical angles as in (6) for a three-dimensional problem. The numerical integration may add a significant portion of the computational work such that an efficient numerical integration scheme is needed. Klein (1999) has developed an icosahedron-based integration scheme for three-dimensional problems, while more sophisticated schemes can be found in Bažant (1986). For simplicity, we use 10-point Gaussian integration scheme by mapping the domains of integration to $[-1,1]$ for each angle in the present study, i.e., there are 100 Gaussian integration points for the double integral with respect to spherical angles θ and ϕ in three dimension, and 10 Gaussian integration points with respect to polar angle ϕ in two dimension. We have also divided the domain of integration for each angle into several (e.g., 4) subintegrals and used 10-point Gaussian integration for each subintegral. The error associated with the 10-point Gaussian integration scheme for each angle (θ or ϕ) is on the order of 0.1%.

The numerical integration scheme with respect to the bond angles has also been tested against the intrinsic symmetry of the VIB model. For example, the moduli given by the general VIB model should not depend on any rigid body rotation $\mathbf{R}$ in the deformation gradient $\mathbf{F}$. The Gaussian integration scheme discussed above gives an error on the order of 0.1% in moduli for different rigid body rotations. For the isotropic VIB model, the moduli given in (29) do not guarantee the Cauchy symmetry, though our numerical results have shown that the Cauchy symmetry holds within an error of 0.1%. These provide further validations of the numerical integration scheme.

4.4 Determination of the Crack Tip Location

Fracture is modeled as strain localization in the VIB model, and is characterized by the vanishing of the determinant of the acoustical tensor $\mathbf{Q}(\mathbf{N})$ in (13). This is implemented in the finite element analysis by examining all directions $\mathbf{N}$ around all Gaussian integration points in all elements at each time (loading) step. Once (13) is met at a Gaussian integration point, crack nucleation (or propagation) starts, and the corresponding $\mathbf{N}$ represents the direction for crack propagation. This provides a means to determine the crack tip location in the VIB model.

4.5 Material Softening

The static VIB model can be unstable due to material softening in the cohesive model. This class of problems must be solved either dynamically or with the aid of artificial damping. The finite element program ABAQUS provides an automatic mechanism for stabilizing unstable static problems through the automatic addition of volume-proportional damping to the model. The mechanism is triggered by including a STABILIZE parameter on any nonlinear static procedure. Viscous forces of the form $\mathbf{F}_v = c\mathbf{M}\mathbf{v}$ are added to the global equilibrium equation, where $\mathbf{M}$ is an artificial mass matrix, c is a damping coefficient, $\mathbf{v}$ is the vector of nodal velocities. The VIB model is stable at the beginning of the step and instabilities may develop in the course of the step. While the model is stable, viscous forces and viscous energy dissipated are very small. If a local region becomes unstable, the local velocities increase such that part of the strain energy then released is dissipated by the applied damping. The damping coefficient, c, is calculated based on the solution of the first increment of the step. Increments in strain energy and in viscously dissipated energy are calculated and extrapolated to the total step time. The damping coefficient is then determined in such a way that the dissipated energy is a small fraction of the strain energy, less than 2.0×10^{-4}.

4.6 Validation

In order to validate the numerical procedures and algorithms, we have calculated several cases that have closed-form solutions. At small deformation, the VIB model degenerates to linear elasticity. Our numerical results have reproduced analytical solutions in linear elasticity, including the crack tip K-field, pure bending of a beam, and stress concentration around a hole. For finite deformation, the numerical results have reproduced all available analytic solutions, including uniaxial, biaxial and triaxial stretching (Gao and Klein, 1998) and pure shear in the VIB model. We have also validated the results against the numerical example for interfacial debonding in multi-layered material systems (Gao and Klein, 1998).

5 Numerical Results

We have studied three examples under static loading using the VIB model. No separate, external fracture criteria are needed for crack nucleation nor for crack growth since fracture becomes a coherent part of the VIB constitutive model. It is not necessary to specify the parameter A, bond density D_0 and unstretched bond length l_0 in the VIB model since they always appear together in the form of shear modulus μ in (17). We have fixed the critical stretch B of the bond in the VIB model as 0.02, giving a localization strain $\varepsilon^* = 2\%$. Once the localization strain is reached, the microscopic bond exceeds the critical stretch B such that the bond has essentially little or no load-carrying capacity, which gives very small tractions, if not vanishing, in severely stretched elements.

5.1 Crack Nucleation from the Stress Concentration around a Hole

The first example is crack nucleation from the stress concentration around a hole. A square plate containing a circular hole is subjected to remote uniaxial tension along its edges in the x_2 direction. The plate is thin in the thickness (x_3) direction and thus can be modeled as a plane-stress problem. The maximum remote strain applied in the stretching direction is $(\varepsilon_{22}^\infty)_{max} = 3 \times 10^{-3}$, much smaller than the localization strain (2%) such that the remote field never fractures.

A plate of $20a \times 20a$ centered around the hole is meshed for the finite element method, where a is the radius of the hole. Only a quarter of the region is analyzed due to symmetry. There are 4355 nodes and 8468 3-node triangular elements, although we have used refined meshes as well as 6-node quadratic elements and 4-node bilinear elements to ensure that there is no mesh dependency.

Figure 3(a) shows the initial, undeformed mesh near the stress concentration around the hole, while Figures 3(b) and 3(c) show the deformed mesh of the same region

as well as the crack tip location at the remote strain $\varepsilon_{22}^{\infty} = 0.275985\%$ and $\varepsilon_{22}^{\infty} = 0.275990\%$, respectively. At $\varepsilon_{22}^{\infty} = 0.275985\%$, several elements along the symmetry plane have been severely stretched and the crack tip has propagated from the hole by a distance approximately equal to the hole radius [Figure 3(b)]. The large difference between small remote $\varepsilon_{22}^{\infty}$ (0.275985%) and large strain near the hole (> localization strain 2%) reflects the strain concentration around the hole. Figure 3(c) shows the deformed mesh at the remote strain $\varepsilon_{22}^{\infty} = 0.275990\%$. It is observed that, even though the remote strain increases only slightly from that in Figure 3(b) (0.275985%), many more elements on the symmetry plane have been severely stretched, and the crack tip has propagated approximately three times the hole radius. Figure 3(d) presents the deformed mesh of the entire region at the remote strain $\varepsilon_{22}^{\infty} = 0.3\%$, which clearly shows all elements on the symmetry plane have been severely stretched and the crack has propagated through the entire specimen.

Figure 3(e) shows the crack length, normalized by the hole radius, versus the remote applied strain $\varepsilon_{22}^{\infty}$, where the crack length is measured from the hole surface. It is observed that, for strains less than 0.27598%, the crack is nucleated and propagated for a short distance less than half of the hole radius. However, as the remote strain exceeds this critical strain level, the crack rapidly propagates through the entire specimen (nearly 10 times the hole radius) for a very small increase in the remote strain. This is rather similar to material instability or unstable crack growth.

5.2   Kinking and Propagation of a Mode II Crack

The second example is the kinking of a mode II crack and the subsequent propagation of the kinked crack. A semi-infinite crack in an infinite solid is subjected to remote K_{II} field. As the remote load increases, the crack will kink out and propagate away from the crack plane.

A circular region containing a crack is meshed by the finite element method. There are 2421 nodes and 4716 3-node triangular elements. The classical K_{II} field is imposed at the outer boundary by prescribing the displacements. Even though a mode II crack is anti-symmetric about the crack plane, this symmetry breaks down as soon as the crack kinks out. Therefore, we do not impose any symmetry conditions in the present analysis.

Figure 4(a) shows the initial, undeformed mesh around the crack tip, and the symmetry about the crack plane is clearly observed. As the remote load K_{II} increases, the deformed mesh becomes unsymmetric. As shown in Figure 4(b) for a relatively small remote load K_{II}, the elements that are approximately $70°$ (clockwise) from the crack plane seem to undergo larger deformation than elsewhere, and the crack tip just kinks out of the initial crack plane. This angle of $70°$ in Figure 4(b) is consistent with the predicted crack kinking angle in mode II based on a maximum crack tip energy release rate criterion in elastic fracture mechanics. The crack kinking and subsequent crack propagation is better shown in Figure 4(c) for a larger remote load K_{II}, where a layer of elements undergoes significantly stretches, indicating that a mode II crack first kinks out at $70°$, then propagates away. It should be pointed out that, this kink angle of $70°$ does not apply to subsequent crack propagation because the tip of the kinked crack is not mode II anymore. At the same remote load K_{II} as in Figure 4(c), the deformed mesh of the entire domain and the kinked crack tip are shown in Figure 4(d), where the crack kinking and propagation are evident from the layer of significantly stretched elements.

5.3   Buckling-Driven Delamination of a Thin Film

A thin film that is bonded to a substrate and subjected to a compressive stress may delaminate by a mechanism involving buckling (e.g., Chai *et al*, 1981; Evans and Hutchinson, 1984; Argon *et al*, 1989; Hutchinson *et al*, 1992; Thouless *et al*, 1992; Huang *et al*, 1998). Once the compressive stress in the film reaches a critical value, the film buckles and the elastic energy stored in the system is released, which then drives the initial delamination to propagate between the film and the substrate, i.e., the so-called "buckling-driven delamination". Hutchinson *et al* (1992) have developed a model to investigate the buckling-driven delamination for a thin film under axisymmetric compression. The initially delaminated portion of the film is modeled as a clamped plate under compression, while the subsequent propagation of the delaminated region is controlled by the crack tip energy release rate. Thouless *et al* (1992) have extended the analysis of buckling-driven delamination to films under the plane-strain condition. The analytical models are in excellent agreement with experiments (Hutchinson *et al*, 1992; Thouless *et al*, 1992).

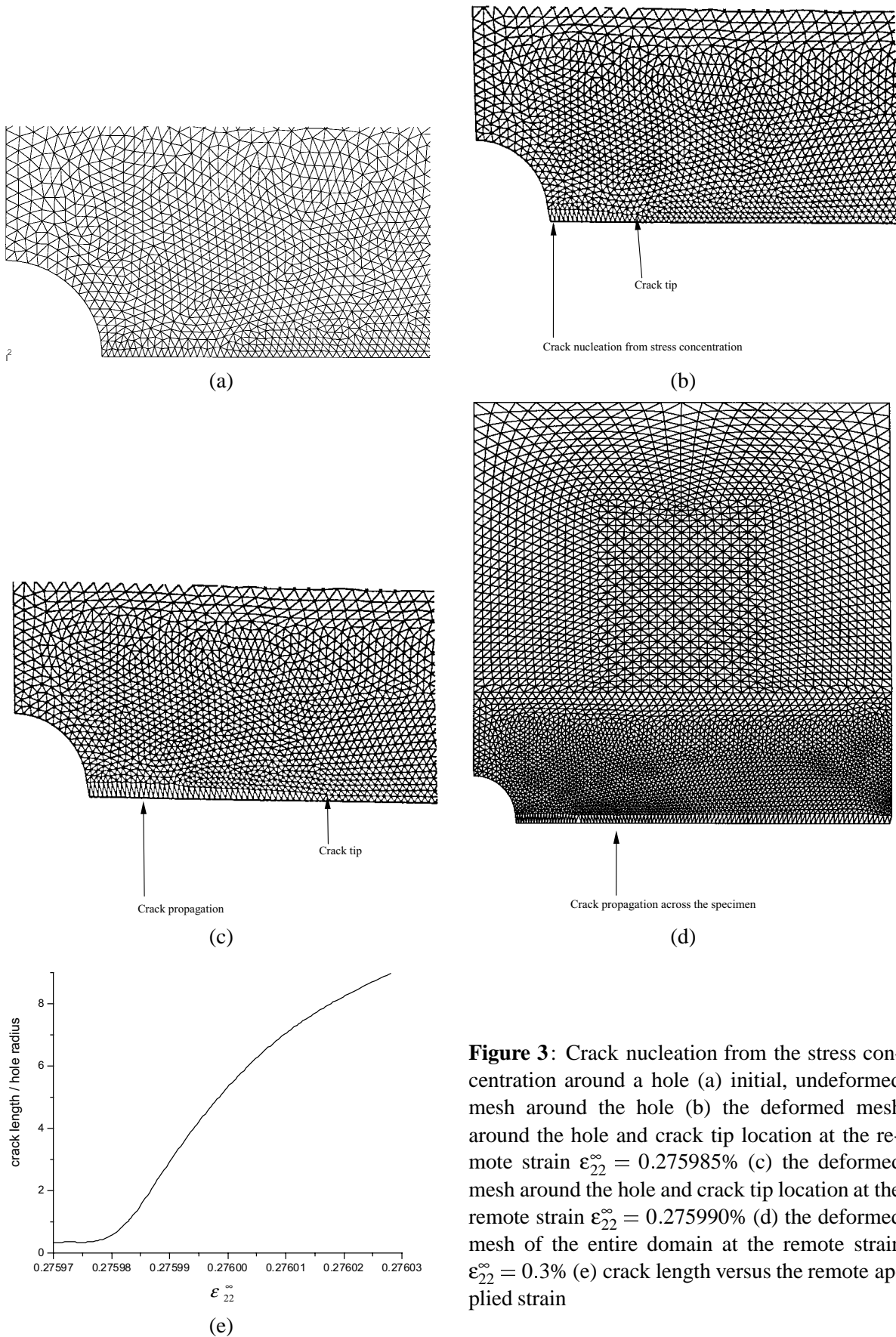We use the VIB model to simulate this buckling-driven delamination in this section. A thin film of thickness *h*

(a)

Crack tip

Crack nucleation from stress concentration
(b)

Crack tip

Crack propagation
(c)

Crack propagation across the specimen
(d)

(e)

Figure 3: Crack nucleation from the stress concentration around a hole (a) initial, undeformed mesh around the hole (b) the deformed mesh around the hole and crack tip location at the remote strain $\varepsilon_{22}^{\infty} = 0.275985\%$ (c) the deformed mesh around the hole and crack tip location at the remote strain $\varepsilon_{22}^{\infty} = 0.275990\%$ (d) the deformed mesh of the entire domain at the remote strain $\varepsilon_{22}^{\infty} = 0.3\%$ (e) crack length versus the remote applied strain
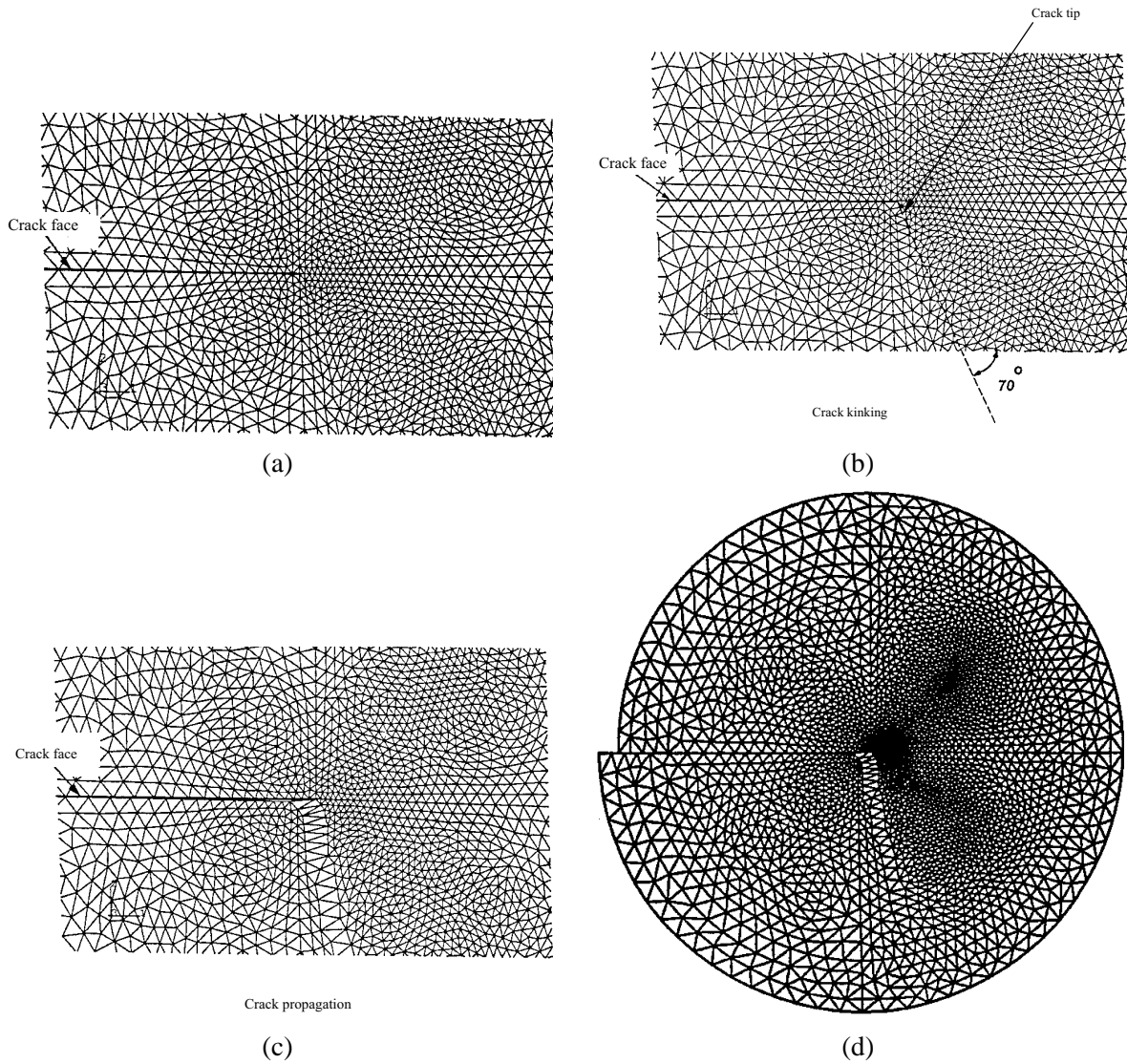
(a)

(b)

(c)

(d)

Figure 4 : Crack kinking and subsequent propagation of a mode II crack (a) initial, undeformed mesh around the crack tip (b) the deformed mesh around the crack tip showing crack kinking around 70° from the crack plane and the tip of the kinked crack (c) the deformed mesh around the crack tip showing subsequent crack propagation (d) the deformed mesh for the entire domain showing subsequent crack propagation and the tip of the kinked crack
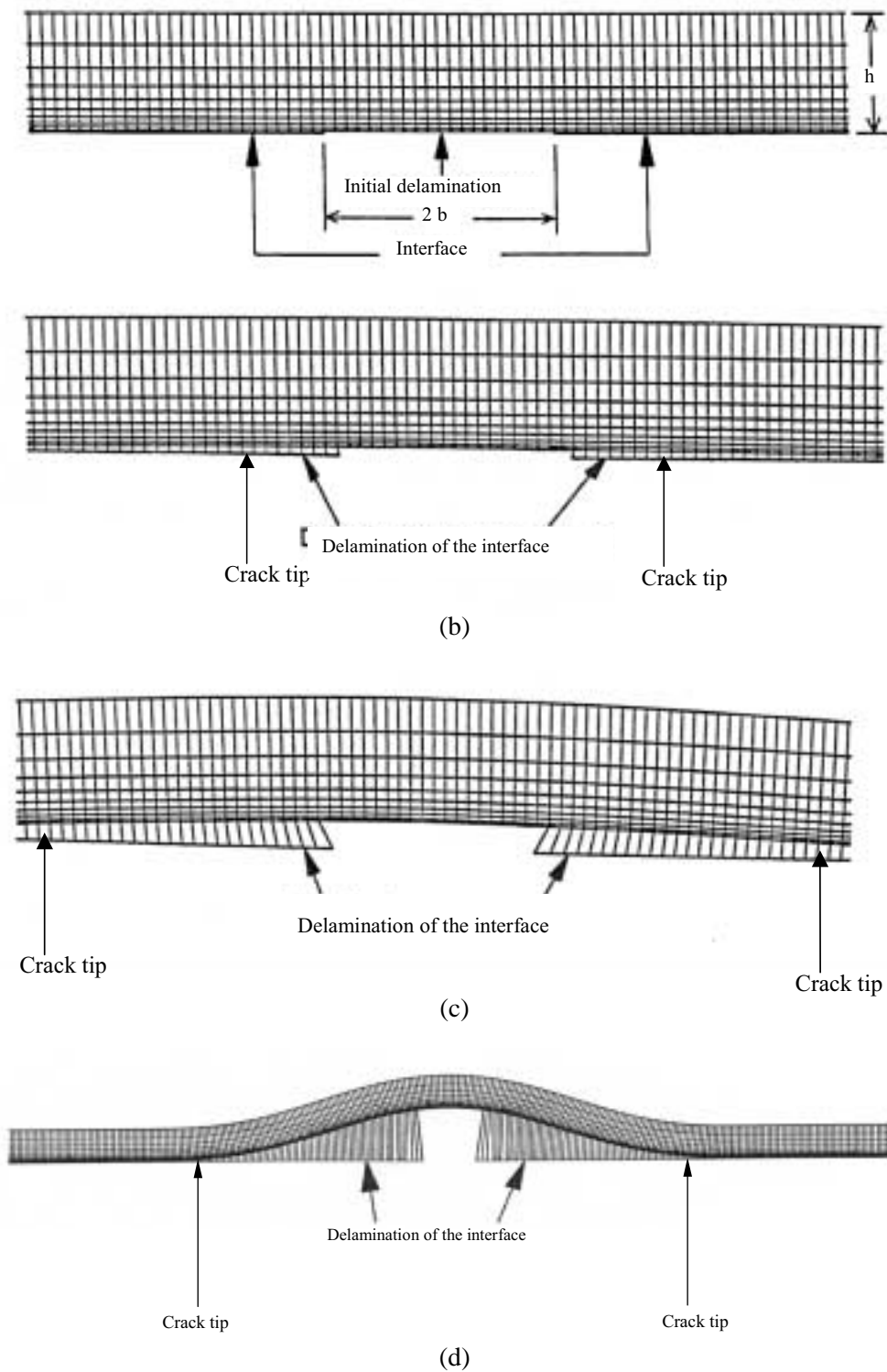
Figure 5 : Buckling-driven delamination of a thin film from the substrate (a) initial, undeformed mesh around the initial delamination (b) the deformed mesh around the initial delamination and the crack tip location at the compressive strain $\varepsilon_0 = 3.237\%$ (c) the deformed mesh around the initial delamination and the crack tip location at the compressive strain $\varepsilon_0 = 3.239\%$ (d) the deformed mesh of the film and the crack tip location at the compressive strain $\varepsilon_0 = 3.243\%$

is bonded to a rigid substrate. The film is initially delaminated from the substrate over a length of $2b$ [Figure 5(a)], but is bonded well to the substrate elsewhere. The length of the initial delamination is twice the film thickness in the present study, i.e., $2b = 2h$, representing a small damage at the interface. The film, characterized by the VIB model, is under compression within its plane, with the remote compressive strain denoted by ε_0. The film is meshed for the finite element methods, with 4612 nodes and 4600 4-node bilinear elements. The rigid substrate has no deformation, and therefore only enters the analysis through the boundary conditions at the interface.

Figure 5(a) shows the undeformed mesh near the initial delamination. Since our interest is the propagation of delamination along the interface, we simplify the initial delaminatin as a very thin slit with the height $0.02\,h$, rather than an interface crack. Figures 5(b) and 5(c) show the deformed mesh around the initial delamination and the crack tip location at the remote compressive strain $\varepsilon_0 = 3.237\%$ and $\varepsilon_0 = 3.239\%$, respectively. The elements at the interface are gradually stretched as the load increases, while elements elsewhere have very little deformation. This clearly indicates the propagation of interface delamination due to film buckling (away from the substrate). This buckling-driven delamination can be better seen in Figure 5(d), where the deformed mesh of a much larger region and the crack tip location are shown at the remote compressive strain $\varepsilon_0 = 3.243\%$. The elements at the interface are severely stretched, indicating interface delamination, while elements elsewhere remain intact. The dark zone just above the elements at the interface in Figure 5(d) is a region of very dense mesh. It should be pointed out that the interface delamination occurs rather rapidly when the compressive strain is around 3% since the strain levels in Figures 5(b), 5(c) and 5(d) are very close. This level of compressive strain 3%, however, is sensitive to the critical stretch B of the bond.

6 Summary

The virtual-internal-bond (VIB) model has incorporated a cohesive-type law into the constitutive model such that the failure of solid becomes a coherent part of the constitutive law. No separate failure criteria need to be prescribed, and a deformation analysis can predict crack nucleation and propagation in materials.

A numerical algorithm suitable for the VIB model under static loading is developed and implemented in the finite element program ABAQUS in this study. We have applied the method to investigate three examples, including crack nucleation and propagation from stress concentration around a hole, the kinking and subsequent propagation of a mode II crack, and the buckling-driven delamination of a thin film from a substrate.

References

Armero, F. and Garikipati, K. (1996): Analysis of strong discontinuities in multiplicative finite strain plasticity and their relation with the numerical simulation of strain localization is solids. *Phys Rev B*, vol. 33, pp. 2863-2885

Argon, A.S.; Gupta, V.; Landis, H.S. and Cornie, J.A. (1989): Intrinsic toughness of interfaces between SiC coatings and substrates of Si or C fibre. *J Mater Sci*, vol. 24, pp. 1207-1218

Barenblatt, G.I. (1959): The formation of equilibrium cracks during brittle fracture: General ideas and hypotheses, axially symmetric cracks. *Appl Math Mech (PMM)*, vol. 23, pp. 622-636

Bažant, Z.P. (1986): Efficient numerical integration on the surface of a sphere. *Zeitschrift fur Angewandte Mathematik und Mechanik*, vol. 66, pp. 37-49

Camacho, G.T. and Ortiz, M. (1996): Computational modeling of impact damage in brittle materials. *Int J Solids Struct*, vol. 33, pp. 2899-2938

Chai, H.; Babcock, C.D. and Knauss, W.G. (1981): One dimensional modeling of failure in laminated plates by delamination buckling. *Int J Solid Struct*, vol. 17, pp. 1069-1083

Dugdale, D.S. (1960): Yielding of steel sheets containing slits. *J Mech Phys Solids*, vol. 8, pp. 100-104

Espinosa, H.D.; Zavattieri, P.D. and Dwivedi, S.K. (1998): A finite deformation continuum discrete

model for the description of fragmentation and damage in brittle materials. *J Mech Phys Solids*, vol. 46, pp. 1909-1942

Evans, A.G. and Hutchinson, J.W. (1984): On the mechanics of delamination and spalling in compressed films. *Int J Solid Struct*, vol. 20, pp. 455-466

Gao, H. and Klein, P. (1998): Numerical simulation of crack growth in an isotropic solid with randomized internal cohesive bonds. *J Mech Phys Solids*, vol. 46, pp. 187-218

Geubelle, P.H. and Baylor, J.S. (1998): Impact-induced delamination of composites: A 2D simulation. *Composites Part B*, vol. 29B, pp. 589-602

Hill, R. (1962): Acceleration waves in solids. *J Mech Phys Solids*, vol. 10, pp. 1-16

Huang, Y.; Liu, C.; Stout, M.G. and Hwang, K.C. (1998): The effect of interfacial damage on the microbuckling of fiber-reinforced composites. *Key Eng Mater*, vol. 145-149, pp. 473-478

Hutchinson, J.W.; Thouless, M.D. and Liniger, E.G. (1992): Growth and configurational stability of circular, buckling-driven film Delaminations. *acta metall mater*, vol. 40, pp. 295-308

Klein, P. and Gao, H. (1998): Crack nucleation and growth as strain localization in a virtual-bond continuum. *Eng Fracture Mech*, vol. 61, pp. 21-48

Klein, P. (1999): *A virtual internal bond approach to modeling crack nucleation and growth*. Ph.D. Dissertation, Stanford University, Palo Alto, CA 94305

Klein, P. and Gao, H. (2000): Study of crack dynamics using the virtual internal bond method. In *Multiscale deformation and fracture in materials and structures, James R. Rice's 60th Anniversary Volume*. Kluwer Academic Publishers, Dordrecht, The Netherlands, pp. 275-309

Marsden, J.E. and Hughes, T.J.R. (1983): *Mathematical Foundations of Elasticity*. Prentice-Hall, Englewood Cliffs, New Jersey

Milstein, F. (1980): Review: Theoretical elastic behaviour of crystals at large strains. *J Mat Sci*, vol. 15, pp. 1071-1084

Simo, J.C. and Taylor, R.L. (1991): Quasi-incompressible finite density in principle stretches. *Comp Mehtods Appl Mech Eng*, vol. 85, pp. 273-310

Tadmor, E.B.; Ortiz, M. and Phillips, R. (1996): Quasicontinuum analysis of defects in solids. *Phil Mag A*, vol. 73, pp. 1529-1563

Thouless, M.D.; Hutchinson, J.W. and Liniger, E.G. (1992): Plane-strain, buckling-driven delamination of thin filmes: Model experements and mode-II fracture. *acta metall mater*, vol. 40, pp. 2639-2649

Tijssens, M.G.A.; Sluys, B.L.J. and van der Giessen, E. (2000): Numerical simulation of quasi-brittle fracture using damaging cohesive surfaces. *Eur J Mech A - Solid*, vol. 19, pp. 761-779

Truesdell, C. and Noll, W. (1965): The non-linear field theories of mechanics. In *Handbuch der Physik, Band iii/3*, Springer, Berlin

Tvergaard, V. and Hutchinson, J.W. (1992): The relation between crack growth resistance and fracture process paramenters in elastic-plastic solids. *J Mech Phys Solids*, vol. 40, pp. 1377-1397

Tvergaard, V. and Hutchinson, J.W. (1993): The influence of plasticity on mixed mode interface toughness. *J Mech Phys Solids*, vol. 41, pp. 1119-1135

Willis, J.R. (1967): A comparison of the fracture criteria of Griffith and Barenblatt. *J Mech Phys Solids*, vol. 15, pp. 151-162

Xu, X.-P. and Needleman, A. (1994): Numerical simulations of fast crack growth in brittle solids. *J Mech Phys Solids*, vol. 42, pp. 1397-1434

Appendix

The fourth order tensor **T** in (29) is (Klein, 1999)

$$\mathbf{T}^{(A)} = \frac{\partial \mathbf{M}^{(A)}}{\partial \mathbf{C}}, \qquad T_{IJKL}^{(A)} = \frac{\partial M_{IJ}^{(A)}}{\partial C_{KL}}, \qquad (34)$$

which is presented separately in the following for three dimension and for two dimension. It is assumed that the tensor **C** has distinct eigenvalues.

(i) three dimension:

$$
\begin{aligned}
\mathbf{T}^{(A)} = {} & \frac{1}{D_A}\left[\mathbf{I} - \mathbf{1}\otimes\mathbf{1}\right] \\
& - \frac{I_3}{D_A\lambda_A^2}\left[\mathbf{I}_{C^{-1}} - \left(\mathbf{C}^{-1} - \mathbf{M}^{(A)}\right)\otimes\left(\mathbf{C}^{-1} - \mathbf{M}^{(A)}\right)\right] \\
& + \frac{\lambda_A^2}{D_A}\left[\left(\mathbf{1}\otimes\mathbf{M}^{(A)} + \mathbf{M}^{(A)}\otimes\mathbf{1}\right)\right. \\
& \left. + \left(I_1 - 4\lambda_A^2\right)\mathbf{M}^{(A)}\otimes\mathbf{M}^{(A)}\right],
\end{aligned}
\tag{35}
$$

where $I_1 = \lambda_1^2 + \lambda_2^2 + \lambda_3^2$ and $I_3 = \lambda_1^2\lambda_2^2\lambda_3^2$ are the trace and determinant of $\mathbf{C}$, respectively, $D_A = 2\lambda_A^4 - \lambda_A^2 I_1 + \frac{I_3}{\lambda_A^2}$, $\mathbf{I}$ is the fourth order identity tensor $[I_{IJKL} = \frac{1}{2}(\delta_{IK}\delta_{JL} + \delta_{IL}\delta_{JK})]$, $\mathbf{1}$ is the second order identity tensor ($1_{IJ} = \delta_{IJ}$), $\mathbf{C}^{-1} = \sum\limits_{B=1}^{3}\frac{1}{\lambda_B^2}\mathbf{N}^{(B)}\otimes\mathbf{N}^{(B)}$ is the inverse of $\mathbf{C}$, and $\mathbf{I}_{C^{-1}}$ is given by

$$
\begin{aligned}
\mathbf{I}_{C^{-1}} &= -\frac{\partial\mathbf{C}^{-1}}{\partial\mathbf{C}}, \\
(I_{C^{-1}})_{IJKL} &= -\frac{\partial C_{IJ}^{-1}}{\partial C_{KL}} = C_{IR}^{-1}\frac{\partial C_{RS}}{\partial C_{KL}}C_{SJ}^{-1} \\
&= \frac{1}{2}(C_{IK}^{-1}C_{JL}^{-1} + C_{IL}^{-1}C_{JK}^{-1}).
\end{aligned}
\tag{36}
$$

(ii) two dimension:

$$
\begin{aligned}
\mathbf{T}^{(A)} = {} & \\
& \frac{\lambda_1^2\lambda_2^2}{\lambda_A^2\left(2\lambda_A^2 - \lambda_1^2 - \lambda_2^2\right)}\left[\mathbf{I}_{C^{-1}} - \left(\mathbf{C}^{-1} - \mathbf{M}^{(A)}\right)\otimes\left(\mathbf{C}^{-1} - \mathbf{M}^{(A)}\right)\right] \\
& - \frac{\lambda_A^2}{2\lambda_A^2 - \lambda_1^2 - \lambda_2^2}\mathbf{M}^{(A)}\otimes\mathbf{M}^{(A)},
\end{aligned}
\tag{37}
$$

where $\mathbf{I}_{C^{-1}}$ is also given in (36), and $\mathbf{C}^{-1} = \sum\limits_{B=1}^{2}\frac{1}{\lambda_B^2}\mathbf{N}^{(B)}\otimes\mathbf{N}^{(B)}$ is the inverse of $\mathbf{C}$.